Phys Chem Minerals (2004) 31: 421–428
DOI 10.1007/s00269-004-0414-y

ORIGINAL PAPER

Y. Lee · J. A. Hriljac · T. Vogt

Pressure-induced migration of zeolitic water in laumontite

Received: 25 October 2003/Accepted: 31 May 2004

Abstract A polycrystalline sample of natural laumontite (Pleasant Valley, Connecticut) was studied up to 6.8 (1) GPa at room temperature using monochromatic synchrotron X-ray powder diffraction and a diamond-anvil cell. A methanol: ethanol: water mixture was used as a penetrating pressure-transmitting fluid. A dry sample measured before adding the pressure fluid inside the diamond-anvil cell contained ~12 H_2O per formula unit, consistent with the water content of partially dehydrated laumontite. Upon increasing the pressure to 0.2 (1) GPa, fully hydrated laumontite with 18 H_2O per unit cell formed and the unit-cell volume expanded by 2.6%. Further pressure increase up to 2.4 (1) GPa resulted in a gradual contraction of the unit-cell volume and individual cell lengths. During this process, a successive order–disorder transition of hydrogen-bonded water molecules from their symmetry sites was observed, concomittent with an inflectional behavior of the monoclinic beta angle and the channel ellipticity. Above 3 GPa, a tripling of the *b* axis was detected. Thereafter, up to 6.8 (1) GPa, the compression behavior was reversed for the *c* axis length and the monoclinic beta angle which showed a gradual increase and decrease, respectively, without any apparent volume discontinuity. We suspect that different ordering of the water molecules or Ca cations inside the channels along the *b* axis may be responsible for the observed supercell transition above 3 GPa.

Keywords High pressure · Laumontite · Hydration · Phase transition · Order–disorder

Y. Lee · T. Vogt (✉)
Physics Dept., Brookhaven National Laboratory,
Upton, New York 11973-5000, USA
E-mail: yollee@bnl.gov, tvogt@bnl.gov
Tel.: +1-631-344-8485
Fax: +1-631-344-2739

J. A. Hriljac
School of Chemistry, The University of Birmingham,
Birmingham, B15 2TT, UK

Introduction

Laumontite, $Ca_4Al_8Si_{16}O_{48}{\cdot}nH_2O$ (space group C2/*m*), is a naturally occurring Ca zeolite which is one of the most common rock-forming zeolites and used as an index mineral for zeolite facies metamorphism (Coombs et al. 1959). Its framework structure is characterized by chains of four-ring and six-ring tetrahedral secondary building units (SBU 6–2, Baerlocher et al. 2001) alternating along the *c* axis to form ten-ring channels (Armbruster and Gunter 2001). These channels contain Ca cations and variable amounts of Ca-coordinating and hydrogen-bonded water molecules. When exposed to relative low humidity (i.e., < 60%) at room temperature, fully hydrated laumontite, which contains 18 water molecules per formula unit (Artioli and Stahl 1993), loses part of its hydrogen-bonded water molecules from the channels and becomes a partially dehydrated laumontite (Artioli et al. 1989; Armbruster and Kohler 1992), formerly referred to as leonhardite. Numerous structural studies of its dehydration and rehydration mechanisms as a function of the relative humidity (Yamazaki et al. 1991; Fridriksson et al. 2003), temperature (Artioli et al. 1996; Stahl et al. 1996), and different exchangeable cations (Kiseleva et al. 1996) have been reported. The effect of hydrostatic pressures on the structure and water stoichiometry, especially when a pore-penetrating pressure medium such as alcohol–water mixture is used, is not known yet. We have recently demonstrated that insertion of high-pressure water into the structural channels occurs in varying degree in natrolite-type zeolites (Lee et al. 2002) and is the key to understanding their anomalous structural and transport changes (Belitsky et al. 1992; Moroz et al. 2001). In natrolite, the structural water content doubles above 1.5 GPa, leading to a volume expansion by ca. 2.5% and enhancement of diffusive mobility of water, whereas in mesolite, a smaller volume expansion by ca. 0.5% under hydrostatic pressures accompanies disordering of Ca and Na cations inside the channels. By performing

comparative studies on edingtonite and thomsonite in connection with the natrolite results, we have shown that different connectivities of the same structural building units also affect their initial water contents under ambient conditions and overall framework responses under hydrostatic pressures (Lee et al. 2004). Here we report the structures of laumontite under hydrostatic pressures mediated by an alcohol and water mixture.

Experimental method

In situ high-pressure synchrotron X-ray powder diffraction experiments were performed using a diamond-anvil cell (DAC) at the X7A beamline at the National Synchrotron Light Source (NSLS) at Brookhaven National Laboratory (BNL). The primary white beam from the bending magnet is focused in the horizontal plane by a triangular, asymmetrically cut Si (111) monochromator bent to a cylindrical curvature by applying a load to the crystal tip, affording microfocused (~200 μm) monochromatic radiation of ~0.7 Å (Lemonnier et al. 1978). A tungsten wire crosshair was positioned at the center of the goniometer circle and subsequently the position of the incident beam was adjusted to the crosshair. A gas-proportional position-sensitive detector (Smith 1991) was stepped in 0.25° intervals over the angular range of 3–35° in 2θ with counting times of 90–150 s per step. The wavelength of the incident beam (0.6639 (1) Å), PSD zero channel, and PSD degrees/channel were determined from a CeO_2 standard (SRM 674). Powdered sample of the single-crystal laumontite (Pleasant Valley, Connecticut, NMNH R4159) was loaded into the DAC at ambient pressure and room temperature along with a few small ruby chips. The DAC is based on a modified Merrill–Bassett design (Merrill and Bassett 1974) and employs two diamonds with 0.5-mm diameter culets on tungsten-carbide supports. The X-rays are admitted by a 0.5-mm diameter circular aperture, and the exit beam leaves via a 0.5×3.0-mm rectangular tapered slit, oriented perpendicular to the horizontal plane of the diffractometer. The sample chamber is provided by a ~200-μm hole made using a spark-erosion method in the center of a 250-μm-thick stainless-steel gasket, pre-indented to 100 μm thickness before erosion. Ambient pressure data were taken without pressure medium inside the DAC. The DAC was placed on the second axis of the diffractometer, and the sample position was adjusted using a pre-centered microscope. A mixture of 16 : 3 : 1 by volume of methanol : ethanol : water was then added as a pressure-transmitting fluid. This alcohol and water mixture is known to remain hydrostatic up to ~10 GPa (Hazen and Finger 1982). The pressure at the sample was measured by detecting the shift in the R1 emission line of the included ruby chips (Bell and Mao 1979). No evidence of nonhydrostatic conditions or pressure anisotropy was detected during our experiments, and the R1 peaks from three included ruby chips remained strong and sharp with deviations in the measured pressure of less than ± 0.1 GPa. Typically, the sample was equilibrated for about 15 min or more at each measured pressure. Several repeated sample grindings and loadings were needed in order to get data with less pronounced texture effects. In the final run, the measurements were done up to 6.8 (1) GPa. The resulting variable pressure powder diffraction patterns are shown in Fig. 1. The recovered sample maintained

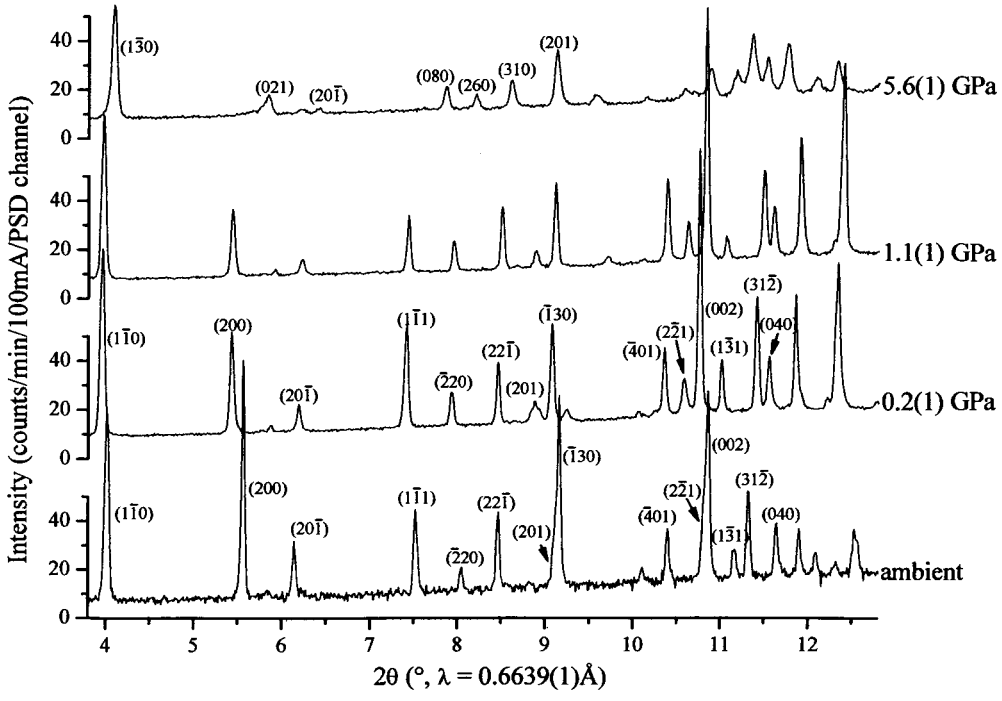

Fig. 1 Details of the changes in the synchrotron X-ray powder diffraction patterns observed for laumontite as a function of pressure

Table 1 Rietveld refined structural models of laumontite at hydrostatic pressures at room temperature[a]

	Ambient	0.2 GPa	0.3 GPa	0.6 GPa	1.1 GPa	1.7 GPa	2.4 GPa
a (Å)	14.7514(9)	14.8831(8)	14.8913(8)	14.8795(10)	14.8486(8)	14.7934(8)	14.7204(13)
b (Å)	13.0827(8)	13.1820(7)	13.1661(7)	13.1442(9)	13.1211(7)	13.0979(6)	13.1084(10)
c (Å)	7.5648(4)	7.5387(3)	7.5284(3)	7.5078(3)	7.4774(3)	7.4420(3)	7.4080(5)
β (°)	111.997(5)	110.181(4)	110.008(4)	109.920(4)	110.001(4)	110.166(4)	110.512(7)
V (Å^3)	1353.6(1)	1388.2(1)	1386.9(1)	1380.5(1)	1368.9(1)	1353.6(1)	1338.8(2)
$_wR_p$, χ^2	0.059, 3.87	0.039, 14.2	0.043, 7.88	0.047, 8.07	0.045, 10.5	0.041, 6.21	0.054, 4.13
Si1 x	0.2412(6)	0.2434(6)	0.2422(6)	0.2407(6)	0.2398(6)	0.2405(5)	0.2444(6)
y	0.3798(3)	0.3825(5)	0.3821(4)	0.3803(4)	0.3813(4)	0.3823(4)	0.3815(4)
z	0.1644(10)	0.1628(11)	0.1598(10)	0.1587(10)	0.1576(11)	0.1610(9)	0.1664(10)
$U_{(iso)}$[b]	0.007(2)	0.038(2)	0.026(2)	0.036(2)	0.038(2)	0.053(2)	0.013(3)
Si2 x	0.0879(6)	0.0794(7)	0.0792(6)	0.0767(7)	0.0743(7)	0.0768(6)	0.0815(6)
y	0.3843(3)	0.3865(5)	0.3872(4)	0.3871(5)	0.3869(5)	0.3859(4)	0.3866(4)
z	0.3346(11)	0.3273(12)	0.3260(11)	0.3233(11)	0.3172(12)	0.3191(10)	0.3200(10)
Al x	0.1317(5)	0.1255(7)	0.1275(6)	0.1278(6)	0.1293(6)	0.1309(6)	0.1308(6)
y	0.3104(6)	0.3097(7)	0.3105(6)	0.3077(6)	0.3095(7)	0.3112(6)	0.3111(6)
z	0.7285(10)	0.7316(12)	0.7293(11)	0.7282(10)	0.7284(11)	0.7312(10)	0.7348(11)
O1 x	0.259(1)	0.272(1)	0.270(1)	0.265(1)	0.266(1)	0.265(1)	0.263(1)
y	0.500	0.500	0.500	0.500	0.500	0.500	0.500
z	0.217(2)	0.215(3)	0.210(2)	0.197(3)	0.208(3)	0.224(2)	0.230(3)
O2 x	0.215(1)	0.202(1)	0.206(1)	0.209(1)	0.212(1)	0.213(1)	0.215(1)
y	0.364(1)	0.369(1)	0.367(1)	0.360(1)	0.365(1)	0.371(1)	0.370(2)
z	0.938(1)	0.935(1)	0.933(1)	0.933(1)	0.931(1)	0.932(1)	0.935(1)
O3 x	0.152(1)	0.137(1)	0.139(1)	0.136(1)	0.134(1)	0.138(1)	0.139(1)
y	0.390(1)	0.389(1)	0.390(1)	0.389(1)	0.389(1)	0.390(1)	0.390(1)
z	0.561(1)	0.554(1)	0.552(1)	0.550(1)	0.545(1)	0.547(1)	0.551(1)
O4 x	0.152(1)	0.156(1)	0.152(1)	0.150(1)	0.146(1)	0.149(1)	0.154(1)
y	0.338(1)	0.349(1)	0.349(1)	0.349(1)	0.349(1)	0.344(1)	0.339(1)
z	0.220(2)	0.230(2)	0.222(2)	0.220(2)	0.209(2)	0.213(2)	0.219(2)
O5 x	0.339(1)	0.336(1)	0.334(1)	0.334(1)	0.331(1)	0.333(1)	0.340(1)
y	0.318(1)	0.315(1)	0.314(1)	0.317(1)	0.315(1)	0.315(1)	0.316(1)
z	0.290(2)	0.275(2)	0.279(2)	0.284(2)	0.284(2)	0.283(2)	0.287(2)
O6 x	0.056(1)	0.040(1)	0.040(1)	0.037(2)	0.036(1)	0.039(1)	0.048(1)
y	0.500	0.500	0.500	0.500	0.500	0.500	0.500
z	0.261(2)	0.257(3)	0.251(2)	0.250(2)	0.241(3)	0.246(2)	0.236(2)
O7 x	0.010(1)	0.007(1)	0.009(1)	0.011(1)	0.013(1)	0.014(1)	0.013(1)
y	0.317(1)	0.305(1)	0.308(1)	0.307(1)	0.306(1)	0.308(1)	0.313(1)
z	0.710(2)	0.724(2)	0.724(2)	0.731(2)	0.737(2)	0.735(2)	0.740(2)
Ca x	0.282(1)	0.269(1)	0.267(1)	0.270(1)	0.270(1)	0.269(1)	0.277(1)
y	0.500	0.500	0.500	0.500	0.500	0.500	0.500
z	0.770(3)	0.733(2)	0.726(2)	0.735(2)	0.725(2)	0.722(2)	0.709(3)
W1 x		0.026(5)	0.024(6)	0.000	0.000	0.000	0.002(9)
y		0.140(3)	0.155(3)	0.153(3)	0.154(3)	0.154(3)	0.175(4)
z		0.047(7)	0.046(7)	0.000	0.000	0.000	0.065(11)
occu.		0.5(8j)	0.5(8j)	1.0(4g)	1.0(4g)	1.0(4g)	0.5(8j)
W2 x	0.409(4)	0.594(2)	0.413(2)	0.409(3)	0.414(2)	0.420(2)	0.438(3)
y	0.448(4)	0.500	0.500	0.500	0.500	0.500	0.500
z	0.016(8)	–0.021(4)	0.011(5)	0.013(4)	0.031(5)	0.039(4)	0.153(6)
occu.	0.5(8j)	1.0(4i)	1.0(4i)	1.0(4i)	1.0(4i)	1.0(4i)	1.0(4i)
W5 x	0.500	0.500	0.500	0.500	0.500	0.500	0.500
y	0.463(6)	0.500	0.500	0.500	0.500	0.500	0.576(5)
z	0.500	0.500	0.500	0.500	0.500	0.500	0.500
occu.	0.5(4h)	1.0(2c)	1.0(2c)	1.0(2c)	1.0(2c)	1.0(2c)	0.5(4h)
W8 x	0.131(3)	0.143(2)	0.140(2)	0.146(2)	0.139(2)	0.134(1)	0.122(2)
y	0.094(2)	0.126(2)	0.122(2)	0.122(2)	0.123(2)	0.126(2)	0.126(2)
z	0.333(5)	0.371(3)	0.365(3)	0.366(3)	0.377(3)	0.378(3)	0.369(5)
occu.	0.76(3)(8j)	1.0(8j)	1.0(8j)	1.0(8j)	1.0(8j)	1.0(8j)	1.0(8j)

[a]Esd's are in parentheses. All sites are fully occupied unless indicated. Multiplicity/Wyckoff letters for sites W1, W2, W5, and W8 are in parenthesis next to their occupancies. Bond restraints used were Si–O = 1.620 (1) Å, Al–O = 1.750 (1) Å, O–O = 2.646 (5) Å (Si-tetrahedra), O–O = 2.858(5)Å (Al-tetrahedra)

[b]Constraints were used to set isotropic displacement parameters the same for all the atoms

its original white color and crystallinity. Rietveld structure analyses (Rietveld 1969) were performed using a starting model of Fridriksson et al. (2003) and data measured up to 2.4 (1) GPa. For the data between 3.4 (1) and 6.8 (1) GPa, whole-pattern fittings using the LeBail method (LeBail et al. 1988) were used to get unit-cell lengths and volumes of the supercell phase (see Discussion below). The diffraction peaks were modeled

Table 1 (contd.) Results from LeBail fits on the supercell phase above 3 GPa and the phase after full pressure release

	4.2 GPa	5.6 GPa	6.8 GPa	Released
a (Å)	14.421(2)	14.225(1)	14.138(2)	14.7437(5)
b (Å)	39.329(6)	38.744(3)	38.469(5)	13.0695(4)
c (Å)	7.374(1)	7.3908(6)	7.3965(8)	7.5467(2)
β (°)	109.98(1)	109.808(6)	109.64(1)	111.841(3)
V (Å^3)	3930.5(6)	3832.4(4)	3788.6(5)	1349.8(1)

by varying three Gaussian half-width parameters, one Lorentzian broadening, and one asymmetry term in the pseudo-Voigt profile function (Thompson et al. 1987). During Rietveld analyses, preferred orientation along the [0 0 1] axis was modeled using the March–Dollase correction (Dollase 1986), and bond-distance restraints were used on Si/Al tetrahedra throughout the refinement. All refinements were performed using the GSAS suite of programs (Larson and VonDreele 1986; Toby 2001) and the results are summarized in Tables 1 and 2. Bulk moduli were calculated by fitting the Birch–Murnaghan equation of state to the normalized volumes ($V/V_0 = [1 + K'P/K_0]^{-1/K'}$, where $K' = (\partial K/\partial P)_{P=0} = 4$) (Angel 2000).

Results and discussion

The pressure-dependent changes of the unit-cell lengths, monoclinic beta angle, and volume of laumontite are displayed in Fig. 2. There is ca. 2.6% unit-cell volume increase between ambient pressure and the first applied pressure of 0.2 (1) GPa. As shown from the Rietveld analysis (Table 1) this is due to an increase in the water content from ca. 12 to 18 per unit cell. The original water content is as expected for a partially dehydrated laumontite under the laboratory humidity conditions (dry powder under ~25% relative humidity) and it goes to a fully hydrated state upon pressurizing (wet powder with alcohol + water pressure-transmitting fluid inside DAC). A similar hydration pathway was studied previously using a controlled humidity chamber, and a volume expansion of ca. 2.3% was recorded at 27 mbar P_{H2O}, leading to 17 H_2O per formula unit from 14 H_2O (Fridriksson et al. 2003). From this point on, increase in pressure results in a gradual decrease of the unit-cell volume up to the final pressure of 6.8 (1) GPa (Fig. 2c). Above 3 GPa, however, the measured diffraction patterns show a tripling of the b axis, and there is a change in the compression behaviors of the individual axis lengths and monoclinic beta angle (Fig. 2a, b). The material transforms back to the ambient phase upon pressure release and exposure to atmosphere.

The structural model of dry laumontite at ambient pressure shows 12.1 (2) H_2O per formula unit with the W1 site empty (Fig. 3). This site is known to be the least occupied site in partially dehydrated phase (Fridriksson et al. 2003) and the first site to dehydrate in the fully hydrated structure (Stahl et al. 1996). The water molecules are distributed in the sites W5, W2, and W8 in the order of increasing population (Table 1). The water molecules at the W2 and W8 sites coordinate Ca cations whereas those at the W5 site form hydrogen bond to framework oxygen and water molecules at the W8 site (Table 2), which is also typical for the partially dehydrated structure. Upon compression to 0.2 (1) GPa using an alcohol + water pressure-transmitting fluid, all water sites, including the previously empty W1 site, become fully occupied (with 50% statistical distribution for the W1 site with the 0.8 (1) Å separation), leading to 18 H_2O per formula unit (Fig. 3). The Ca cation becomes seven coordinated by one and two water molecules from the W2 and W8 sites, respectively, along with four oxygen atoms from the framework. The water molecules at the W1 and W5 sites hydrogen bond to the Ca-coordinating water molecules or framework oxygens. It is interesting to note that under these conditions the statistically distributed water molecules at the W2 and W5 sites merge into a mirror plane and a 2/m site in the center of the channel, respectively (Fig. 3 and Table 1). Such ordering of the Ca-coordinating W2 site has been reported to occur with full hydration (Fridriksson et al. 2003) but that of the hydrogen-bonded W5 site has not been observed before. Further increase of pressure to 0.6 (1) GPa results in a similar site ordering of the water molecules at the W1 site into a two fold site (Fig. 3 and Table 1). This progressive ordering of the hydrogen-bonded water molecules at the W5 and W1 sites can be linked to changes in the framework geometry due to the increasing compression. Concomitant with the full hydration and ordering of the W2 and W5 sites at 0.2 (1) GPa, the monoclinic distortion angle decreases abruptly (Fig. 2b). Further compression results in a continued decrease of the beta angle up to 0.6 (1) GPa, where the W1 water molecules become ordered. During this process, the opening of the channel along the c-axis becomes less elliptical (Fig. 4). Then above 0.6 (1) GPa, the monoclinic beta angle and the channel ellipticity increase continuously (Figs. 2b, 4), and at 2.4 (1) GPa, the hydrogen-bonded water molecules at the W1 and W5 sites split back to the statistical distributions (Fig. 3). The increase of the [0 0 1] channel ellipticity with pressure pushed the W1 water molecules toward the acute angle of the channel. The W1–O7 bond distance is continuously reduced with increasing pressure [from 2.92 (6) Å at 0.2 (1) GPa to 2.38 (7) Å at 2.4 (1) GPa, Table 2] whereas W2 water molecules move away from Ca-coordination [from 2.41 (3) Å at 0.2 (1) GPa to 2.63 (3) Å at 1.7 (1) GPa, Table 2], approaching to the middle of the channels, and at 2.4 (1) GPa a new nonframework topological configuration energetically favorable is observed (Fig. 3). The coordination of non-framework cation as well as water molecules changes significantly during this re-entrant order–disorder transitions (Fig. 3 and Table 2). In the ordered state between 1 and 2 GPa, water molecules at

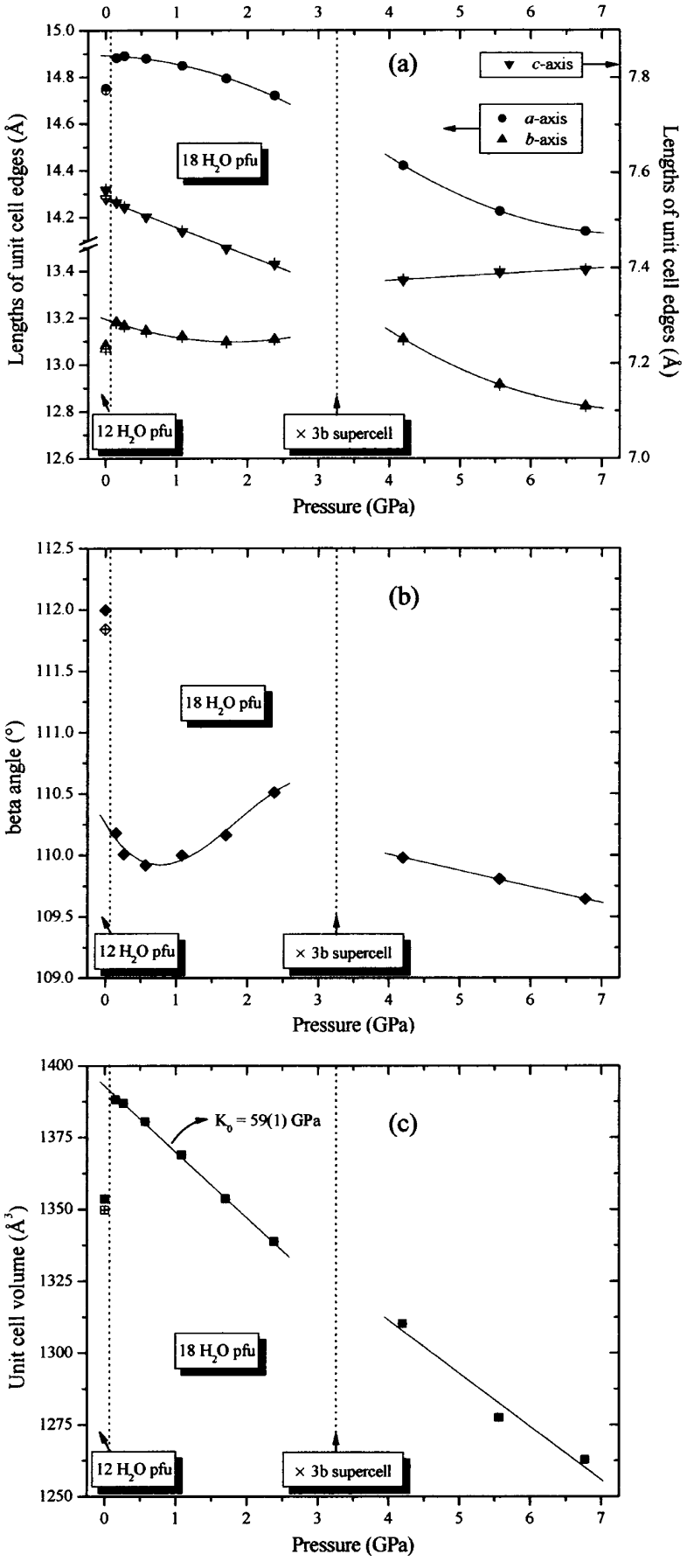

Fig. 2a–c Pressure dependence of **a** unit-cell edge lengths, **b** monoclinic beta angle, and **c** unit-cell volume of laumontite. Open symbols represent data after pressure release. Continuous lines are guides to the eye (bulk modulus was obtained from a fit to the normalized cell-volume data using second-order Birch-Murnaghan equation of state, see text)

Table 2 Selected interatomic distances and angles of laumontite at hydrostatic pressures at room temperature[a]

	Ambient	0.2 GPa	0.3 GPa	0.6 GPa	1.1 GPa	1.7 GPa	2.4 GPa
Si1–O1	1.619(2)	1.618(4)	1.620(3)	1.618(3)	1.618(3)	1.616(2)	1.619(2)
Si1–O2	1.618(2)	1.621(4)	1.618(3)	1.616(3)	1.618(3)	1.619(2)	1.620(2)
Si1–O4	1.620(2)	1.620(4)	1.620(3)	1.618(3)	1.619(3)	1.619(2)	1.620(2)
Si1–O5	1.619(2)	1.617(4)	1.619(3)	1.619(3)	1.620(3)	1.618(2)	1.618(2)
Si2–O3	1.620(2)	1.625(4)	1.626(3)	1.626(3)	1.628(3)	1.621(2)	1.620(2)
Si2–O4	1.620(2)	1.625(4)	1.624(3)	1.623(3)	1.624(3)	1.621(2)	1.621(2)
Si2–O6	1.621(2)	1.628(4)	1.624(3)	1.624(3)	1.623(3)	1.622(2)	1.619(2)
Si2–O7	1.619(2)	1.615(4)	1.620(3)	1.620(3)	1.620(3)	1.618(2)	1.620(2)
Al–O2	1.747(2)	1.752(4)	1.747(3)	1.746(3)	1.744(3)	1.748(2)	1.748(2)
Al–O3	1.748(2)	1.751(4)	1.750(3)	1.750(3)	1.749(3)	1.746(2)	1.747(2)
Al–O5	1.747(2)	1.748(4)	1.747(3)	1.746(3)	1.746(3)	1.747(2)	1.746(2)
Al–O7	1.746(2)	1.745(4)	1.747(3)	1.747(3)	1.745(3)	1.746(2)	1.747(2)
Si1–O1–Si1	152.5(11)	146.1(13)	147.0(11)	152.9(12)	148.3(13)	145.2(11)	147.5(13)
Si1–O2–Al	145.3(7)	150.4(9)	149.0(8)	148.6(8)	144.9(8)	142.2(7)	141.7(7)
Si2–O3–Al	123.4(7)	129.7(7)	128.7(7)	129.7(7)	130.9(7)	129.9(6)	130.9(7)
Si1–O4–Si2	135.0(7)	145.0(9)	144.6(9)	144.7(11)	143.3(10)	139.1(7)	134.9(7)
Si1–O5–Al	128.9(7)	136.9(9)	136.6(8)	132.9(8)	134.6(9)	134.4(8)	130.6(8)
Si2–O6–Si2	138.1(8)	133.6(11)	132.3(9)	132.0(10)	132.2(10)	134.1(8)	133.3(8)
Si2–O7–Al	148.6(8)	134.3(8)	136.6(8)	135.4(9)	133.7(8)	136.2(7)	140.2(8)
Ca–O2	2.59(2)×2	2.70(2)×2	2.69(2)×2	2.71(2)×2	2.68(2)×2	2.63(1)×2	2.76(2)×2
Ca–O3	2.45(2)×2	2.45(1)×2	2.40(1)×2	2.48(2)×2	2.47(2)×2	2.41(1)×2	2.44(2)×2
Ca–W2	2.20(6)×2	2.41(3)	2.47(3)	2.38(3)	2.54(3)	2.63(3)	
Ca–W8	2.12(3)×2	2.41(2)×2	2.37(2)×2	2.31(3)×2	2.39(2)×2	2.46(2)×2	2.42(3)×2
W1–O4			3.20(5)				3.02(8)
W1–O7		2.92(6)	3.10(6)	2.90(3)×2	2.85(3)×2	2.88(3)×2	2.38(7)
			2.81(6)				3.07(6)
W1–W1		0.8(1)[b]	0.8(1)[b]				1.0(2)[b]
W1–W2		2.25(6)	2.34(6)	2.45(4)×2	2.45(3)×2	2.40(3)×2	2.65(6)
		2.52(6)	2.59(6)				3.11(7)
W1–W8		2.47(4)	2.47(5)	2.90(2)×2	2.90(2)×2	2.85(2)×2	2.41(9)
							3.15(10)
W2–O1	3.19(5)	2.85(4)	2.99(4)	2.91(5)	2.92(4)	3.06(3)	2.82(4)
W2–O2	2.92(5)						
W2–O5	3.15(5)						3.14(3)×2
W2–W2	1.35(10)[b]	2.93(7)	2.66(6)	2.80(8)	2.75(7)	2.63(6)	
	2.78(10)						
	3.09(10)						
W2–W5							2.60(4)×2
W2–W8	2.54(6)		3.11(3)×2	3.13(3)×2			3.10(4)×2
	3.13(6)						
W5–O5	2.99(5)×2						2.73(3)×2
W5–W5	0.97(15)[b]						1.98(12)[b]
W5–W8	2.78(4)×2	3.11(2)×4	3.07(2)×4	3.13(3)×4	3.01(2)×4	2.96(2)×4	2.41(3)×2
	3.18(5)×2						
W8–O3	3.00(4)	3.14(2)	3.13(2)	3.09(3)			
W8–O4		3.15(2)		3.18(3)		3.14(2)	3.09(3)
W8–O5	2.96(4)	2.70(2)	2.71(2)	2.67(3)	2.56(2)	2.52(2)	2.53(3)
W8–O7		3.16(2)				3.15(2)	3.08(3)
W8–W8	2.46(6)						

[a]Esd's are in parentheses
[b]Simultaneous occupancy excluded

the W5 site becomes four-connected to surrounding water molecules at the W8 sites. Upon disordering of the W1 and W5 sites above 2 GPa, the Ca cation becomes only six-coordinated by losing a bond to the water molecule at the W2 site (Fig. 3 and Table 2). This contrasts to the seven-fold coordination found in the fully hydrated state below 2 GPa.

As described earlier, the phase above 3 GPa is characterized by a tripling of the *b*-axis, and the axial compression behavior does not follow that of the subcell region. The pressure–volume data, however, do not show any apparent discontinuity (Fig. 2c), implying that the transition to the supercell is not a first-order phase transition. When the bulk modulus is calculated including the supercell data above 3 GPa, the resulting value [$K_0^{\text{overall}} = 58$ (1) GPa] is the same within one sigma as the one calculated using only the subcell data [$K_0 = 59$ (1) GPa]. This transition is likely to be the result of different ordering of water molecules or Ca cations in the channels along the *b*-axis. Intriguingly, this is the opposite behavior to that observed in mesolite, $Na_{5.33}Ca_{5.33}Al_{16}Si_{24}O_{80}{\cdot}21.33H_2O$,

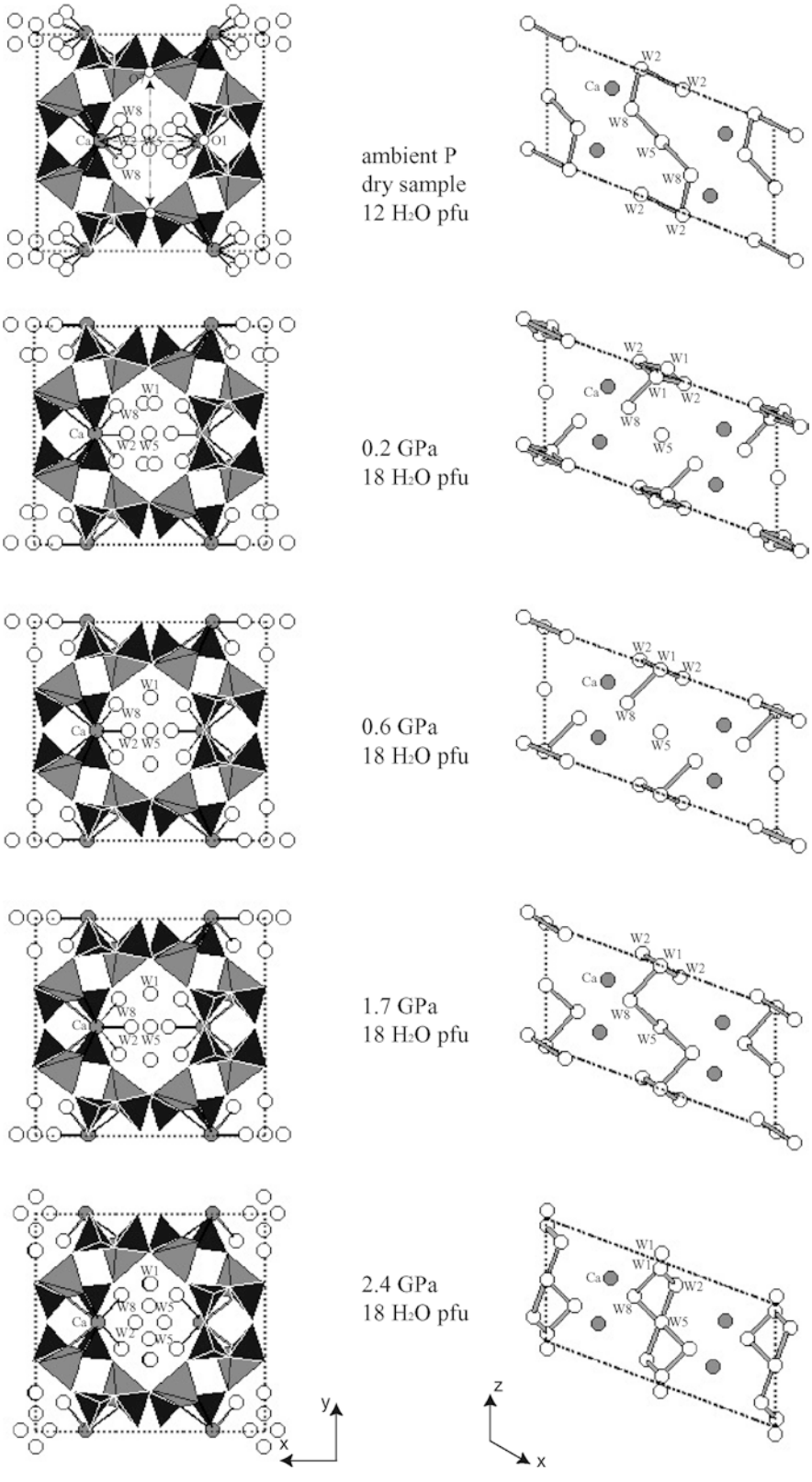

Fig. 3 Crystal structures of laumontite at increasing hydrostatic pressures. On the left polyhedral models are viewed along the *c*-axis. Bars represent Ca–O bondings (within 3.0 Å). Framework tetrahedra are shown in two colors to illustrate Al/Si ordering. On the right arrangements of water molecules and Ca cations are viewed along the *b*-axis. Bars represent hydrogen bondings (within 3.0 Å). Framework tetrahedra are omitted for clarity. Dotted lines represent unit cells (see tables for site ordering, occupancy and bonding distances)

under similar hydrostatic pressure conditions, where the original supercell (3*b*) from a 2 : 1 alternation of Ca and Na layers transforms to the natrolite subcell (*b*) upon pressure-induced hydration above 1.5 GPa (Lee et al. 2002). We suspected that a disordering of Ca and Na cations and a subsequent loss of the layer contrast might be the reason for the loss of the supercell in mesolite. Unfortunately, the present high-pressure powder diffraction data in the laumontite supercell region are not of sufficient quality to allow

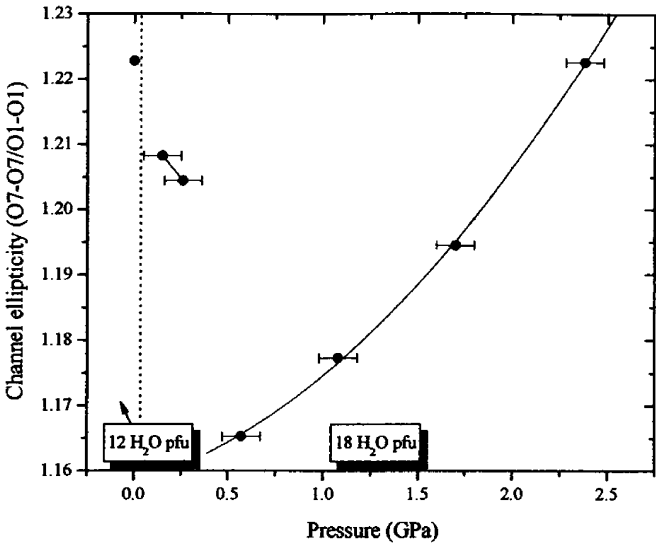

Fig. 4 Pressure dependence of the ellipticity of the channel opening along the *c*-axis (see Fig. 3). Continuous lines are guides to the eye

full structure refinement. Single crystal studies are underway to clarify these issues.

Acknowledgements This work was supported by an LDRD from the Brookhaven National Laboratory (Pressure in Nanopores). J. Hriljac thanks the Royal Society. The authors thank Jeffrey Post of the National Museum of Natural History at the Smithsonian Institution for providing the mineral specimens and Jingzhu Hu of the Geophysical Laboratory of the Carnegie Institute for the access to their ruby laser system at beamline X17C. Research carried out in part at the NSLS at Brookhaven National Laboratory is supported by the U.S, DoE (DE-Ac02–98CH10886 for beamline X7A).

References

Angel RJ (2000) Equations of state. In: Hazen RM, Downs RT, (eds). Reviews in mineralogy and geochemistry: high-temperature and high-pressure crystal chemistry, vol 41, The Mineralogical Society of America, Washington, DC, pp 35–58

Armbruster T, Gunter ME (2001) Crystal structures of natural zeolites. In: Bish DL, Ming DW, (eds) Natural zeolites: occurrence, properties, application, vol 45, Mineralogical Society of America, Washington, DC, pp 1–57

Armbruster T, Kohler T (1992) Rehydration and dehydration of laumontite—a single-crystal X-ray study at 100K. N Jb Mineral-Monhefte (9): 385–397

Artioli G, Stahl K (1993) Fully hydrated laumontite—a structure study by flat-plate and capillary powder diffraction techniques. Zeolites 13 (4): 249–255

Artioli G, Smith JV, Kvick A (1989) Single-crystal neutron-diffraction study of partially dehydrated laumontite at 15K. Zeolites 9 (5): 377–391

Artioli G, Stahl K, Hanson JC (1996) The dehydration process in the natural zeolite laumontite: a real-time synchrotron X-ray powder diffraction study. European powder diffraction: Epdic Iv, Pts 1 and 2, 228, pp 369–374

Baerlocher C, Meier WM, Olson DH (2001) Atlas of zeolite framework types. Elsevier, Amsterdam, pp 16–17

Belitsky IA, Fursenko BA, Gubada SP, Kholdeev OV, Seryotki YV (1992) Structural transformations in natrolite and edingtonite. Phys Chem Miner 18: 497

Bell PM, Mao HK (1979) Absolute pressure measurements and their comparison with the ruby fluorescence (R1) pressure scale to 1.5 Mbar. Carnegie Inst. Washington Year Book, vol 78, pp 665–669

Coombs DS, Ellis AJ, Fyfe WS, Taylor AM (1959) The zeolite facies, with comments on the interpretation of hydrothermal syntheses. Geochim Cosmochim Acta 17: 53–107

Dollase WA (1986) Correction of intensities for preferred orientation in powder diffractometry—application of the March model. J Appl Crystallogr 19: 267–272

Fridriksson T, Bish DL, Bird DK (2003) Hydrogen-bonded water in laumontite I: X-ray powder diffraction study of water site occupancy and structural changes in laumontite during room-temperature isothermal hydration/dehydration. Am Mineral 88: 277–287

Hazen RM, Finger LW (1982) Comparative crystal chemistry. Wiley, New York

Kiseleva I, Navrotsky A, Belitsky IA, Fursenko BA (1996) Thermochemistry of natural potassium sodium calcium leonhardite and its cation-exchanged forms. Am Mineral 81: 668–675

Larson AC, VonDreele RB (1986) GSAS; general structure analysis system. Los Alamos National Laboratory, New Mexico

LeBail A, Duroy H, Fourquet JL (1988) Ab-initio structure determination of $LiSbWO_6$ by powder X-ray diffraction. Mat Res Bull 23: 447–452

Lee Y, Vogt T, Hriljac JA, Parise JB, Artioli G (2002) Pressure-induced volume expansion of zeolites in the natrolite family. J Am Chem Soc 124: 5466–5475

Lee Y, Hriljac JA, Studer A, Vogt T (2004) Anisotropic compression of edingtonite and thomsonite to 6 GPa at room temperature. Phys Chem Mineral 31: 22–27

Lemonnier M, Fourme R, Rosseaux F, Kahn R (1978) X-ray curved-crystal monochromator system at the storage ring DCI. Nucl Instrm Meth 152: 173–177

Merrill L, Bassett WA (1974) Miniature diamond anvil pressure cell for single-crystal X-ray diffraction studies. Rev Sci Instrum 45: 290–294

Moroz NK, Kholopov EV, Belitsky IA, Fursenko BA (2001) Pressure-enhanced molecular self-diffusion in microporous solids. Micropor Mesopor Mater 42: 113–119

Rietveld HM (1969) A profile refinement method for nuclear and magnetic structures. J Appl Crystallog 2: 65–71

Smith GC (1991) X-ray imaging with gas proportional detectors. Synch Rad News 4: 24–30

Stahl K, Artioli G, Hanson JC (1996) The dehydration process in the zeolite laumontite: a real-time synchrotron X-ray powder diffraction study. Phys Chem Miner 23 (6): 328–336

Thompson P, Cox DE, Hastings JB (1987) Rietveld refinement of Dedye-Scherrer synchrotron X-ray data from Al2O3. J Appl Crystallogr 20: 79–83

Toby BH (2001) EXPGUI, a graphical user interface for GSAS. J Appl Crystallogr 34: 210–213

Yamazaki A, Shiraki T, Nishido H, Otsuka R (1991) Phase change of laumontite under relative humidity-controlled conditions. Clay Science 8: 79–86